$O_2(^1\Delta)$ production in high pressure flowing He/O_2 plasmas: Scaling and quenching

Natalia Y. Babaeva[a)]
Department of Electrical and Computer Engineering, Iowa State University, Ames, Iowa 50011

Ramesh Arakoni[b)]
Department of Aerospace Engineering, University of Illinois, Urbana, Illinois 61801

Mark J. Kushner[c)]
Department of Electrical and Computer Engineering, Iowa State University, Ames, Iowa 50011

(Received 24 February 2007; accepted 17 April 2007; published online 22 June 2007)

Chemical oxygen-iodine lasers (COILs) oscillate on the $^2P_{1/2} \rightarrow {}^2P_{3/2}$ transition of atomic iodine at 1.315 μm by a series of excitation transfers from $O_2(^1\Delta)$. In electrically excited COILs (eCOILs), the $O_2(^1\Delta)$ is produced in a flowing plasma, typically He/O_2, at a few to tens of Torr. Many system issues motivate operating eCOILs at higher pressures to obtain larger absolute densities of $O_2(^1\Delta)$ for a given yield and to provide higher back pressure for expansion. In this paper, we discuss results from a computational investigation of $O_2(^1\Delta)$ production in flowing plasmas sustained at moderate pressures ($\leqslant$50 Torr). Power deposition and flow rates were scaled such that in the absence of second order effects, yield should be constant and absolute $O_2(^1\Delta)$ production should scale linearly with pressure. We found in many cases that absolute $O_2(^1\Delta)$ production scaled sublinearly with pressure. Ozone is found to be one of the major quenchers of $O_2(^1\Delta)$ and its production increases with pressure. Gas heating also increases with increasing pressure due to exothermic three-body reactions. The gas heating reduces O_3 production, increases O_3 destruction and, for certain conditions, restores yields. With increasing pressure and increasing absolute densities of atomic oxygen and pooling reactions of $O_2(^1\Delta)$, quenching by these species also becomes important, though the influence of O-atom quenching can be controlled by managing the density of O atoms with additives. The yield of $O_2(^1\Delta)$ is also determined by discharge stability which becomes problematic at higher pressure. © *2007 American Institute of Physics*. [DOI: 10.1063/1.2743878]

I. INTRODUCTION

Chemical oxygen-iodine lasers are being investigated because of their ability to be delivered through optical fibers (1.315 μm), their highly scalable continuous wave power, and favorable material interaction properties.[1–6] Operation of the chemical oxygen-iodine laser (COIL) is based on an electronic transition between the spin-orbit levels of the ground state configuration of the iodine atom, $I(^2P_{1/2}) \rightarrow I(^2P_{3/2})$. The upper level is populated by near resonant energy transfer (quantum defect $\sim$219 cm^{-1}) from $O_2(^1\Delta)$ to ground state $I(^2P_{3/2})$. The COIL generates ground state I atoms by dissociative excitation transfer from $O_2(^1\Delta)$ to I_2. Typically, $O_2(^1\Delta)$ is produced in an external chemical reactor by a gas-liquid reaction between gaseous chlorine and a basic hydrogen peroxide solution[7] producing yields approaching 100% of the oxygen emerging in the $O_2(^1\Delta)$ state. The long lifetime of $O_2(^1\Delta)$ (spontaneous lifetime of about 60 min) and robustness against quenching enables transport over long distances to the laser cavity.

In electrically excited COILs (eCOILs), the $O_2(^1\Delta)$ is produced in a flowing plasma, typically He/O_2, at a few to tens of Torr. Helium is often used as a buffer gas to lower the discharge gas temperature and to provide a more optimum electron temperature for excitation of $O_2(^1\Delta)$. Unlike the conventional COIL, the electric discharge variant also produces atomic oxygen by electron-impact dissociation of molecular oxygen. Although the atomic oxygen is a quencher of the upper laser level, it can also aid in the dissociation of I_2. Recent and ongoing investigations have shown that substantial yields of $O_2(^1\Delta)$ can be generated by an appropriately tailored electric discharge[8–17] in mixtures of O_2 with rare gas diluents. Scaling studies of non-self-sustained discharges where ionization is supported by an external source suggest that $O_2(^1\Delta)$ yields approaching 25%–30% might be possible. This is accomplished by tailoring the electron temperature to more closely match the energy range where the excitation cross sections for $O_2(^1\Delta)$ are largest.[12–14]

The three main components of COIL devices are the $O_2(^1\Delta)$ generator, a supersonic nozzle, and the laser cavity. The primary purpose of the supersonic nozzle is to lower the temperature in the laser cavity, thereby reducing the likelihood of the energy transfer process from $O_2(^1\Delta)$ to $I(^2P_{1/2})$ proceeding in the reverse direction. Recently, positive gain and laser oscillation in atomic iodine in a supersonic flow optical cavity have been reported resulting from electric discharge produced $O_2(^1\Delta)$.[18–21] An overview of $O_2(^1\Delta)$ generation in plasmas is given in Ref. 22.

a)Electronic mail: natalie5@iastate.edu
b)Electronic mail: arakoni@uiuc.edu
c)Author to whom correspondence should be addressed; electronic mail: mjk@iastate.edu

Many system issues motivate operating eCOILs at higher pressures to obtain larger densities of $O_2(^1\Delta)$ for a given yield and to provide higher back pressure for expansion. If higher order effects are not important, and parameters such as energy deposition per molecule are maintained constant, it is expected that absolute $O_2(^1\Delta)$ production [that is, the total number of $O_2(^1\Delta)$ molecules produced] should scale linearly with pressure, thereby providing additional motivation for higher pressure operation.

In previous work, the scaling of production of $O_2(^1\Delta)$ was computationally investigated using global-kinetics, one-dimensional, and two-dimensional (2D) models.[13,14] It was found that the yield of $O_2(^1\Delta)$ generally scaled linearly with energy deposition at low pressures (<10 Torr) until the ground state O_2 is depleted. In this work, we report on results from a computational investigation of radio frequency (rf) excited flowing He/O_2 plasmas using plug-flow and two-dimensional (2D) models. The emphasis is on developing scaling laws for $O_2(^1\Delta)$ production in eCOIL systems when operating at higher pressures. We found that although yields may decrease with increasing pressure, absolute densities of $O_2(^1\Delta)$ typically do increase. Ground state and vibrationally excited ozone are major quenchers of $O_2(^1\Delta)$, and production of these species increase with pressure. With increasing absolute densities of atomic oxygen and pooling reactions of $O_2(^1\Delta)$, quenching by these species also become important, though the influence of O-atom quenching can be minimized by managing the O-atom density with additives. The yield of $O_2(^1\Delta)$ is also determined by discharge stability which becomes problematic at higher pressures.

The models and reaction mechanism are briefly described in Sec. II. The results from our investigations using the plug-flow model are discussed in Sec. III, followed by a discussion of results obtained from the 2D model in Sec. IV. Concluding remarks are in Sec. V.

II. DESCRIPTION OF THE MODELS

This investigation was performed with plug-flow and 2D models. The plug-flow model GLOBAL_KIN addresses gas-phase chemistry and transport, solution of Boltzmann's equation for the electron energy distribution, and equations for axial fluxes of mass, momentum, gas energy, and electron energy. The model is described in detail in Ref. 13 and so will be only briefly discussed here.

GLOBAL_KIN is a volume averaged, global-kinetics model for plasma chemistry. When operated in a plug-flow mode, axial transport is also approximated. GLOBAL_KIN contains a plasma chemistry module, a surface kinetics module, and an electron energy transport module. In the plasma chemistry module, the time rate of change of species and temperatures (electron and gas) are obtained integrating their respective conservation equations. Assuming a linear axial flow in a cylindrical tube, transport to radial surfaces is included by using a diffusion length. The reaction of fluxes on surfaces is addressed by the surface kinetics module which utilizes a surface site-balance model. Electron-impact rate coefficients are provided by the electron energy transport module where the electron energy distributions are obtained by solving Boltzmann's equation. By simultaneously calculating the axial speed of the flow based on constant pressure, change in enthalpy, species densities, and gas temperature, the integration in time is mapped to axial position. Although computationally fast, the weakness of this method is neglecting axial transport by diffusion.

The 2D model used in this study, nonPDPSIM, is a multifluid hydrodynamics simulation, described in detail in Ref. 14, in which transport equations for all charged and neutral species and Poisson's equation are integrated as a function of time. Poisson's equation [Eq. (1)], transport equations for conservation of the charged species [Eq. (2)], and the surface charge balance equation [Eq. (3)] are simultaneously integrated using a Newton iteration technique,

$$-\nabla\cdot(\varepsilon_0\varepsilon_r\nabla\Phi)=\sum_j N_j q_j+\rho_s, \tag{1}$$

$$\frac{\partial N_j}{\partial t}=-\nabla\cdot\mathbf{\Gamma}_j+S_j, \tag{2}$$

$$\frac{\partial \rho_s}{\partial t}=\sum_j q_j(-\nabla\mathbf{\Gamma}_j+S_j)-\nabla\cdot(\sigma[-\nabla\Phi)], \tag{3}$$

where ε_0, ε_r, Φ, ρ_s, N_j, $\mathbf{\Gamma}_j$, σ, S_j, and q_j are the permittivity of free space, dielectric constant, electric potential, surface charge density, species density and flux, conductivity of solid materials, sources, and charge, respectively. The subscripts j denote gas-phase species. Updates of the charged particle densities and electric potential are followed by an implicit update of the electron temperature by solving the electron energy equation for average energy, ε,

$$\frac{\partial(n_e\varepsilon)}{\partial t}=q\mathbf{\Gamma}_e\cdot\mathbf{E}-n_e\sum_j\Delta\varepsilon_j N_j\kappa_j-\nabla\cdot\left(\frac{5}{2}\varepsilon\mathbf{\Gamma}_e-\lambda_e\nabla T_e\right), \tag{4}$$

where $\frac{3}{2}kT_e=\varepsilon$. The terms in Eq. (4) are for the contribution from Joule heating, elastic and inelastic impact processes with heavy neutrals and ions with energy loss κ_j, and electron heat flux consisting of terms for electron energy flux (Γ_e) and a conduction (λ_e is the electron thermal conductivity). The electron transport coefficients and rate coefficients for bulk electrons as a function of T_e are obtained by solving the zero-dimensional Boltzmann's equation for the electron energy distribution to capture the non-Maxwellian nature of the electron swarm.

The fluid averaged advective velocity $\mathbf{v}$ is obtained by solving a modified form of the compressible Navier-Stokes equations in which momentum transfer from ion and electron collisions; and acceleration by the electric field are included in the momentum equation, and Joule heating is included in the energy equations,

$$\frac{\partial\rho}{\partial t}=-\nabla\cdot(\rho\mathbf{v})+P, \tag{5}$$

$$\frac{\partial(\rho\mathbf{v})}{\partial t}=-\nabla p-\nabla\cdot(\rho\mathbf{v}\mathbf{v})-\nabla\cdot\bar{\bar{\tau}}+\sum_j(q_jN_j-M_j\mu_jS_j)\mathbf{E}, \tag{6}$$

$$\frac{\partial(\rho c_p T)}{\partial t} = -\nabla(-\kappa \nabla T + \rho \mathbf{v} c_p T) + \sum_j \mathbf{j}_j \cdot \mathbf{E} - \sum_i R_i \Delta H_i + p \nabla \cdot \mathbf{v}, \quad (7)$$

where P represents the inlet and outlet flows (the inlet flow is specified while the output flow is adjusted to maintain a constant mass flux), ρ is the total mass density, p is the thermodynamic pressure, $\bar{\bar{\tau}}$ is the viscosity tensor, c_p is the heat capacity, κ is the species averaged thermal conductivity, μ is the mobility, and M the molecular weight. ΔH_i is the change enthalpy due to reaction i having total rate R_i. The reactions include Frank-Condon heating from electron-impact dissociation of molecules as well as conventional chemical reactions. The sums (other than for reactions) are over all charged and neutral species. The contributions to momentum from charged particles include those of electrons. The contributions to the energy equation from Joule heating include contributions from ions. The heat transfer from electrons is included as a collisional change in enthalpy. The relationship between pressure, density, and temperature is given by the ideal-gas law. The numerical grid in nonPDPSIM uses an unstructured, cylindrically symmetric mesh with triangular elements.

The reaction mechanism for He/O_2 plasmas used here is essentially the same as that described in Refs. 13 and 14, and involves reactions in the gas-phase discharge and afterglow as well as recombination and quenching reactions on the discharge tube walls. The species in the model are ground-state neutrals O_2, O, O_3, and He; $O_2(v)$ (the first four vibrational levels of O_2), electronic states $O_2(^1\Delta)$, $O_2(^1\Sigma)$, $O(^1D)$, $O(^1S)$, and $He(^2S)$; and the ions O_2^+, O^+, O_2^-, O^-, O_3^-, and He^+.

The precursors to the eCOIL laser, $O_2(^1\Delta)$ (0.98 eV) and $O_2(^1\Sigma)$ (1.63 eV), are dominantly produced in the discharge by direct electron impact with the ground state,

$$e + O_2 \rightarrow O_2(^1\Delta) + e, \quad (8)$$

$$e + O_2 \rightarrow O_2(^1\Sigma) + e, \quad (9)$$

and in reactions of electronic excitation transfer from metastable $O(^1D)$ atoms,

$$O(^1D) + O_2 \rightarrow O_2(^1\Sigma) + O. \quad (10)$$

Production of $O_2(^1\Sigma)$ generally also results in generation of $O_2(^1\Delta)$ through rapid collisional quenching reactions with atomic oxygen and ozone. The atomic oxygen is dominantly produced by electron-impact dissociation of O_2,

$$e + O_2 \rightarrow O + O + e, \quad (11)$$

$$e + O_2 \rightarrow O(^1D) + O + e. \quad (12)$$

The $O_2(^1\Delta)$ persists far into the afterglow due to its long radiative lifetime, where the most significant quenching reactions are collisions with O atoms and O_3, and energy pooling with $O_2(^1\Delta)$. The rate of quenching of $O_2(^1\Delta)$ by collisions with the walls is uncertain due to the variability of the quenching probability with temperature and conditions of the wall. Based on estimates for similar conditions, we have assigned a wall quenching coefficient of 10^{-5}, which results in insignificant wall quenching for typical eCOIL conditions.

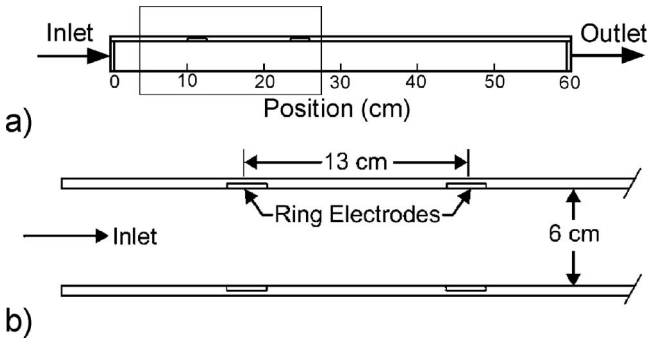

FIG. 1. Schematic of the discharge tube. (a) Computational domain. The flow enters uniformly from the left where pressure, speed, and temperature are specified. The walls are held at constant temperature and mass flux is conserved at the outlet. (b) Close-up showing ring electrodes.

The effective yield of $O_2(^1\Delta)$ is defined as the ratio of the combined $O_2(^1\Delta)$ and $O_2(^1\Sigma)$ densities to the sum of the densities of all oxygen-containing species on a molecular O_2 basis,

$$Y = \frac{[O_2(^1\Delta)] + [O_2(^1\Sigma)]}{([O_2] + [O_2(v)] + [O_2(^1\Delta)] + [O_2(^1\Sigma)] + 0.5[O] + 1.5[O_3])}. \quad (13)$$

This choice of yield was made with the prior knowledge that the majority of $O_2(^1\Sigma)$ is quenched directly to $O_2(^1\Delta)$. Typically in the afterglow region, the density of $O_2(^1\Sigma)$ is negligibly small. As such, Eq. (13) is most relevant for best case energy scaling.

In our model, the first four vibrational states of O_2 are lumped into a single effective vibrational state $O_2(v)$ having excitation energy of 0.19 eV. In addition to superelastic electron collisions with $O_2(v)$, all electron impact processes included for ground state O_2 were also included for $O_2(v)$ with the threshold energy shifted by 0.19 eV. In a similar manner, in addition to collisional quenching of $O_2(v)$ which contributes to gas heating, all heavy particle reactions included for ground state O_2 were also included for $O_2(v)$. Although we acknowledge that rate coefficients for these processes may depend on the vibrational state, there is limited kinetic available to account for those effects and so they have not been included here. Since the density of $O_2(v)$ is typically only $10^{-2}-10^{-3}$ that of ground state O_2 we expect that the error resulting from those omissions is small.

A schematic of the idealized eCOIL device addressed in this study is shown in Fig. 1. A $He/O_2=70/30$ mixture is flowed through a cylindrically symmetric quartz tube 60 cm in length and 6 cm in diameter. A rf electric discharge is operated between two ring electrodes 2 cm wide with centers separated by 13 cm. The electrodes are powered up to a few kW at 25 MHz. The flow rate for each pressure corresponds to an average axial inlet speed of 985 cm/s. Thus the species residence time is approximately the same for each pressure provided we neglect gas heating. Our investigations were limited to the region of the reactor prior to supersonic expan-

sion and injection of I_2. The wall temperature was held fixed at 300 K assuming active water-jacket cooling.

III. SCALING OF $O_2(^1\Delta)$ PRODUCTION WITH PRESSURE: PLUG-FLOW MODELING

The basic scaling laws of $O_2(^1\Delta)$ generation as a function of pressure in flowing He/O_2 plasmas were first investigated using the plug-flow model GLOBAL_KIN for the geometry shown in Fig. 1. To eliminate as many systematic trends as possible while changing pressure, two parameters were kept constant: energy deposition per inlet oxygen molecule α (eV/molecule) and flow residence time in the discharge tube, τ. To keep τ constant, the flow rate is increased in proportion to pressure. To keep α constant, power is increased in proportion to pressure provided τ is constant. Computationally, this is accomplished by computing the power deposition as a cycle averaged product of voltage times current and comparing that power to the value required to keep α constant. Every few rf cycles the voltage is adjusted (increased or decreased by a maximum of a few percent) in the direction to deliver the desired power. This process is continued until a quasi-steady-state is reached.

Keeping these parameters constant, if there are no second order effects, yield should remain constant and absolute $O_2(^1\Delta)$ production should scale linearly with pressure. We also expect that the electron temperature T_e and gas temperature T_g should weakly depend upon pressure. The former insensitivity results from electron losses being dominated by volumetric processes (i.e., attachment and dissociative recombination) and so the rate of loss by diffusion does not significantly affect the electron accounting. The latter insensitivity results from thermal conduction, which is the dominant temperature regulating loss process, not being a sensitive function of pressure in the range we investigated.

At least two second order effects will be seen to be important: three-body reactions and discharge stability. The three-body reactions which produce quenchers of $O_2(^1\Delta)$, such as O_3, are detrimental due to the resulting reduction in $O_2(^1\Delta)$ density. Three-body reactions of the sort $A+B+M \rightarrow AB+M$ are typically exothermic and can be a significant heating source as these reactions begin to dominate at higher pressures. The resulting increase in gas temperature usually has a negative effect. The onset of discharge instabilities at higher pressures is potentially harmful due to the nonuniform power deposition that results.

Plasma parameters obtained with the plug-flow model for pressures from 3 to 50 Torr for $He/O_2=70/30$ and $\alpha=0.3$ eV/molecule (40–670 W) are shown in Figs. 2–5. The power profile is specified based on the results from the 2D model. When keeping α constant, the electron density weakly depends upon pressure, increasing in peak value from 1×10^{10} to 1.9×10^{10} cm^{-3} from 3 to 50 Torr. There is a small decrease in T_e (from 2.7 to 2.4 eV) when increasing pressure due to a reduction in diffusion losses of electrons. The decrease in T_e then reduces the power dissipation per electron which necessitates an increase in electron density.

Electron-impact dissociative excitation of O_2 results in approximately 10% dissociation, producing peak O-atom densities of 2.2×10^{15} to 1.6×10^{16} cm^{-3} from 3 to 50 Torr. This increase in O-atom density is sublinear with respect to pressure due to the increased efficiency of consumption of O atoms by the three-body collisions that form ozone,

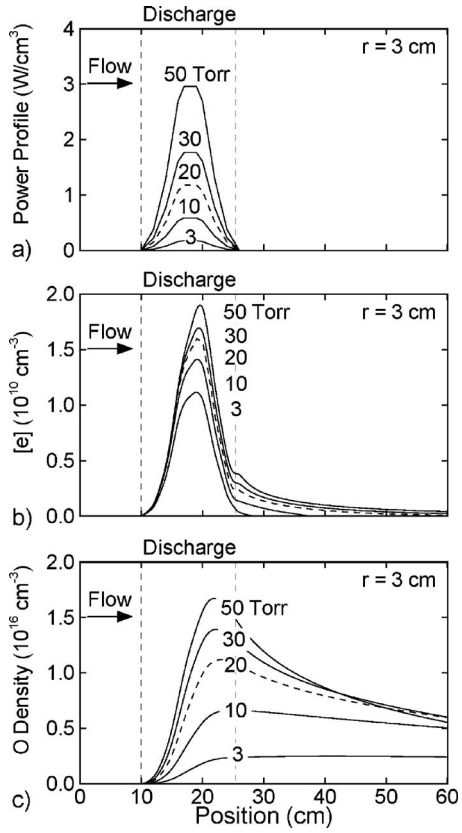

FIG. 2. Plasma and flow parameters for 3–50 Torr ($\alpha=0.3$ eV/molecule, $He/O_2=70/30$, $r=3$ cm). (a) Power, (b) electron density, and (c) atomic oxygen density. In the discharge region up to 10% of the molecular oxygen is dissociated.

$$O + O_2 + M \rightarrow O_3 + M. \quad (14)$$

This reaction has a rate coefficient of $6\times10^{-34}(T_g/300)^{-2.8}$ cm^6 s^{-1} which decreases the formation of ozone with increasing gas temperature. The main reaction for ozone destruction,

$$O + O_3 \rightarrow O_2 + O_2, \quad (15)$$

has a rate coefficient, $8\times10^{-12}\exp(-2060/T_g)$ cm^3 s^{-1}. The increase in exothermic three-body reactions, such as Eq. (14), with increasing pressure results in significant gas heating. In spite of α being a constant, the result is that the peak gas temperature increases from 330 to 520 K when increasing pressure from 3 to 50 Torr. Note that at 3 Torr, the peak in T_g occurs in the discharge region where plasma heating (mostly ion Joule heating) is the dominant heating mechanism. At 50 Torr, T_g peaks downstream, a consequence of heating from exothermic three-body reactions which occur dominantly outside the plasma zone.

The combination of increasing production of O_3 due to three-body processes and increasing destruction of O_3 due to an increase in gas temperature results in the axial dependence of O_3, as shown in Fig. 3(a). At low pressure, the peak in O_3 density occurs downstream. The low rate of three-body

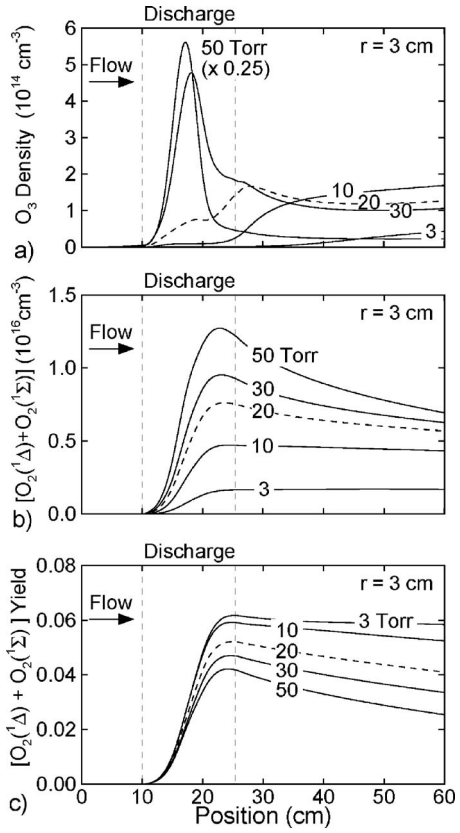

FIG. 3. Density of oxygen species for 3–50 Torr (α=0.3 eV/molecule, He/O_2=70/30, r=3 cm). (a) O_3, (b) $O_2(^1\Delta)+O_2(^1\Sigma)$ and (c) combined $O_2(^1\Delta)+O_2(^1\Sigma)$ yield. The peak of ozone production is in the upstream side of the discharge region where the gas temperature is lower.

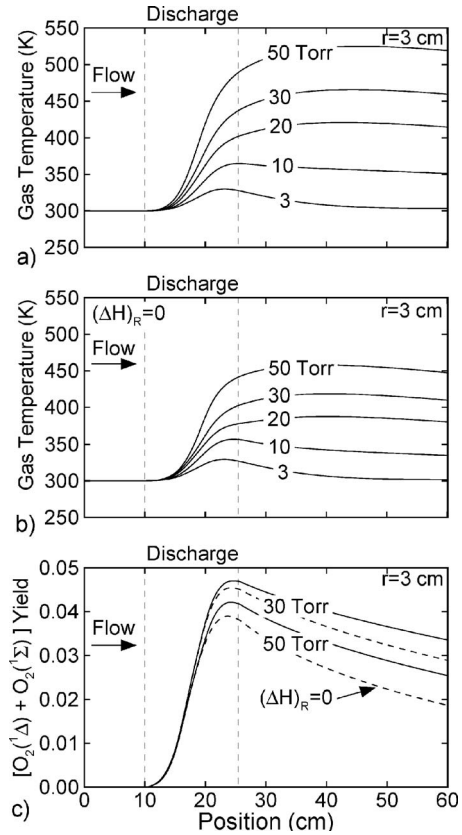

FIG. 5. Gas temperature and yield for 3–50 Torr (α=0.3 eV/molecule, He/O_2=70/30, r=3 cm). (a) Enthalpy from three-body recombination heating is included, (b) recombination heating is excluded, and (c) combined $O_2(^1\Delta)+O_2(^1\Sigma)$ density for 30 and 50 Torr with and without recombination heating. For these conditions there is a decrease in yield when the gas becomes colder due to the increased production of O_3.

reactions and low gas temperature (low rates of O_3 destruction) result in most of the O_3 being produced only after a finite flow time and this density accumulates in the discharge. (The average residence time in the flow tube is 60 ms.) At higher pressures, the rate of three-body reactions

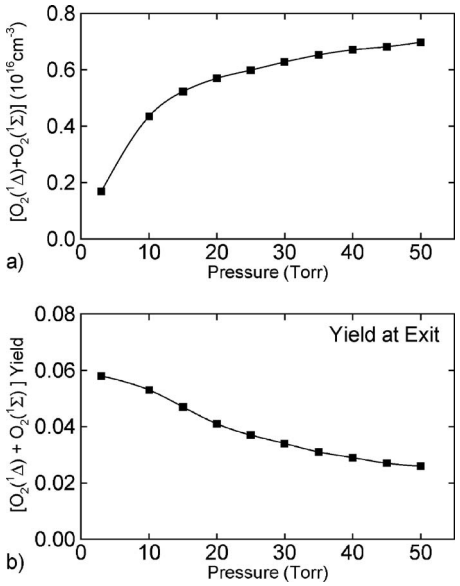

FIG. 4. Density of oxygen species (α=0.3 eV/molecule, He/O_2=70/30, r=3 cm) as a function of pressure at the exit of the tube. (a) $O_2(^1\Delta)+O_2(^1\Sigma)$ and (b) combined $O_2(^1\Delta)+O_2(^1\Sigma)$ yield.

is proportionally higher resulting in large rates of formation of O_3 in the discharge prior to there being significant gas heating. For example, the peak O_3 density is 2.2×10^{15} cm^{-3} at 50 Torr. The accompanying increase in gas temperature downstream results in increased rates of destruction of O_3 by collisions with O atoms which ultimately reduces its density. The end result is that the downstream density of O_3 is maximum at $(1-2)\times10^{14}$ cm^{-3} at pressures of 10–20 Torr.

The O_3 density is an important consideration due to its being an efficient quencher of $O_2(^1\Delta)$,

$$O_2(^1\Delta) + O_3 \rightarrow O_2 + O_2 + O. \tag{16}$$

With a rate coefficient of $5.2\times10^{-11}\exp(-2840/T_g)$ cm^3 s^{-1}, the rate of quenching increases with the increase in gas temperature occurring at higher pressures. [Note that the rate coefficient for quenching of $O_2(^1\Delta)$ by vibrationally excited O_3 is more than an order of magnitude larger than for the ground state.[23]] The increase in O_3 and the increase in gas temperature both increase quenching rates. This results in the density of O_2^* [denoting the sum of the densities of $O_2(^1\Delta)$ and $O_2(^1\Sigma)$] increasing sublinearly with increasing pressure and in the decrease of total yield as a function of pressure, as shown in Fig. 4. At low pressure ($\leqslant$10 Torr) with constant α, the yield is nearly constant and so the absolute production of O_2^* scales with pressure. At

higher pressures, the production and yield of O_2^* peak in the plasma zone. The density of O_2^* decreases thereafter, a consequence of downstream quenching at the higher gas temperatures in the presence of O_3. The result is sublinear scaling with pressure.

At higher pressures contributions to gas heating are dominated by three-body recombination heating and Frank-Condon heating due to dissociative electronic excitation. To distinguish between these two contributions, we artificially excluded contributions to gas heating from changes in enthalpy ΔH from three-body recombination reactions. The resulting gas temperatures, shown in Fig. 5(b), are lower by 50–70 K at higher pressures (30 and 50 Torr). For lower pressures (3–10 Torr) the differences in gas temperature are small and heating is dominated by Frank-Condon and Joule heating in the plasma zone. Decreasing the temperature in this manner increases the O_3 density which translates directly into higher quenching and lower exit densities of O_2^*. This results in lower O_2^* yields, as shown in Fig. 5(c).

The hierarchy of the main quenchers of $O_2(^1\Delta)$ for 10, 30, and 50 Torr is shown in Fig. 6 for the base case conditions. Quenching times are determined by $1/(k[M])$, where $[M]$ is density of the quencher and k is the rate constant. More rapid and important quenching reactions are denoted by shorter quenching times. By the exit of the discharge tube, O_3 is the primary quencher for pressures >10 Torr. For pressures higher than 30 Torr, quenching times by O_3 become comparable to the gas residence time which is about 60 ms. Atomic oxygen is the second most important quencher. Quenching times for O_2 and $O_2(^1\Delta)$ are of the order of a few seconds and not important. Note that the O_3 density, especially at high pressures, is two orders of magnitude smaller than atomic oxygen but it is the dominant quencher.

Another second order effect that complicates pressure scaling when changing the tube size is heat transfer to the walls. For example, plasma and flow parameters for tubes having radii of 3 and 1 cm while keeping other conditions equal (α=0.9 eV/molecule and 60 ms residence time) are shown in Figs. 7 and 8. In the larger tube and with the larger diffusion length for heat transfer to the walls, gas heating at 50 Torr produces temperatures of nearly 800 K. As a consequence, O_3 produced in large quantities upstream in the discharge is rapidly depleted in the afterglow. The prior dominance of O_3 as a quencher is reduced to be comparable to that of atomic oxygen. Yield for O_2^* at the end of the tube for 50 Torr is 10%, down from 14% at 3 Torr.

Reducing the tube radius results in more efficient gas cooling due to the shorter radial diffusion length. For example, the gas temperature at the tube exit at 50 Torr drops from 750 K for a radius of 3 cm to 430 K for a radius of 1 cm. As a result, there is increasing production of O_3 downstream as the temperature decreases, ozone again becomes the main quencher of $O_2(^1\Delta)$, and yield decreases to 7%.

Ozone and gas temperature management are clearly important considerations in pressure scaling. For example, pressure scaling for a tube with a radius of 1 cm was repeated keeping α=0.9 eV/molecule while increasing the flow rate to reduce the residence time by a factor of 9 to approximately 7 ms. The results are shown in Fig. 9. Since α is

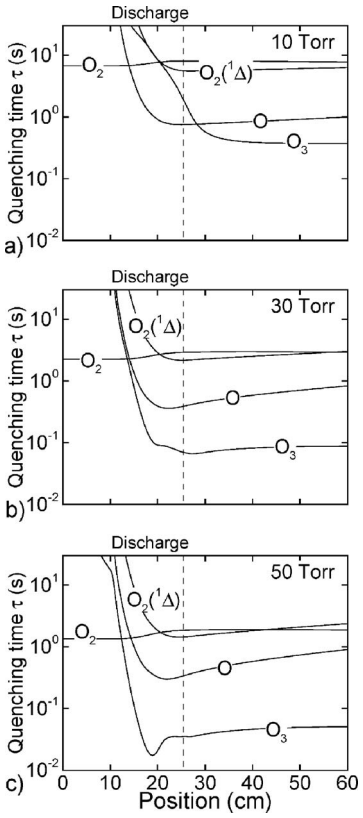

FIG. 6. Quenching times for $O_2(^1\Delta)$ for (a) 10, (b) 30, and (c) 50 Torr (α =0.3 eV/molecule, He/O_2=70/30, r=3 cm). Ozone is the main quencher in the postdischarge downstream region. For pressures higher than 30 Torr the ozone quenching time becomes comparable with the gas residence time.

constant the maximum gas temperature is nearly the same as the prior case. However, the shorter residence time downstream reduces the amount of conductive cooling and so the exit gas temperature increases to 610 K for 50 Torr. The higher gas temperature increases the rate of O_3 destruction and decreases the rate of its formation, thereby reducing O_3 densities. The lower O_3 densities and shorter residence times reduce the likelihood that quenching of $O_2(^1\Delta)$ will occur. As a result, yield is restored to 13.3% at 50 Torr.

Another factor that is potentially important to pressure scaling is the possibility of three-body quenching of $O_2(^1\Delta)$ by O atoms. Previous studies of excited state kinetics in discharges sustained in oxygen[11,15,16] indicated lower than expected yields of $O_2(^1\Delta)$ at higher pressures where the O-atom density is high. The authors[11] proposed that oxygen atoms in a three-body collision were responsible for the quenching,

$$O_2(^1\Delta) + O + O_2 \rightarrow O_2 + O_2 + O. \quad (17)$$

Good agreement was obtained between modeling and experiments with a rate coefficient of 1×10^{-32} cm^6 s^{-1}. This process is in addition to the two-body quenching of $O_2(^1\Delta)$ by O atoms,

$$O_2(^1\Delta) + O \rightarrow O_2 + O, \quad (18)$$

having a rate coefficient of 1.1×10^{-10} cm^3 s^{-1}.

The densities of O_2^* and yields for 10 and 50 Torr with and without three-body O-atom quenching of $O_2(^1\Delta)$ are

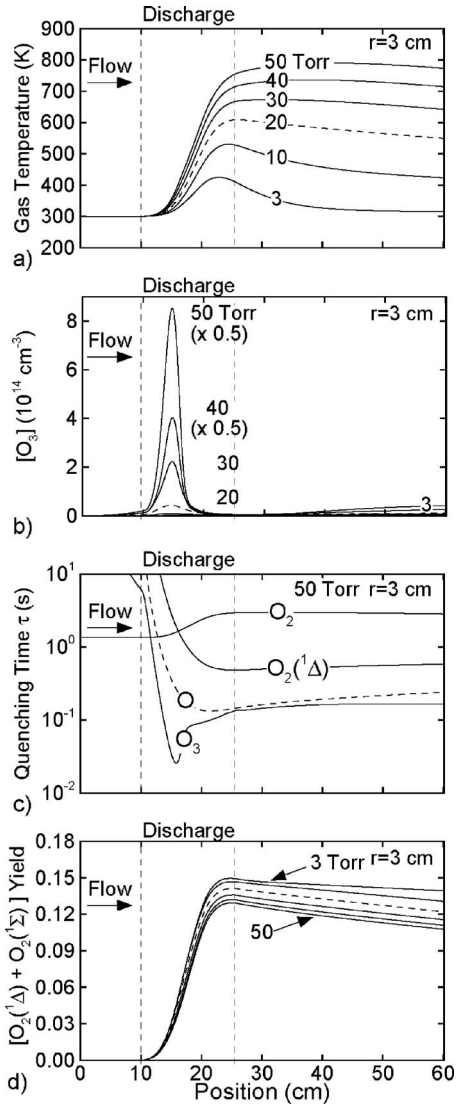

FIG. 7. Plasma and flow parameters for 3–50 Torr (α=0.9 eV/molecule, He/O_2=70/30) for a radius of 3 cm and a residence time of 60 ms. (a) Gas temperature, (b) O_3 density, (c) quenching times at 50 Torr, and (d) combined $O_2(^1\Delta)+O_2(^1\Sigma)$ yield. A long residence time results in higher gas temperature and lower ozone density.

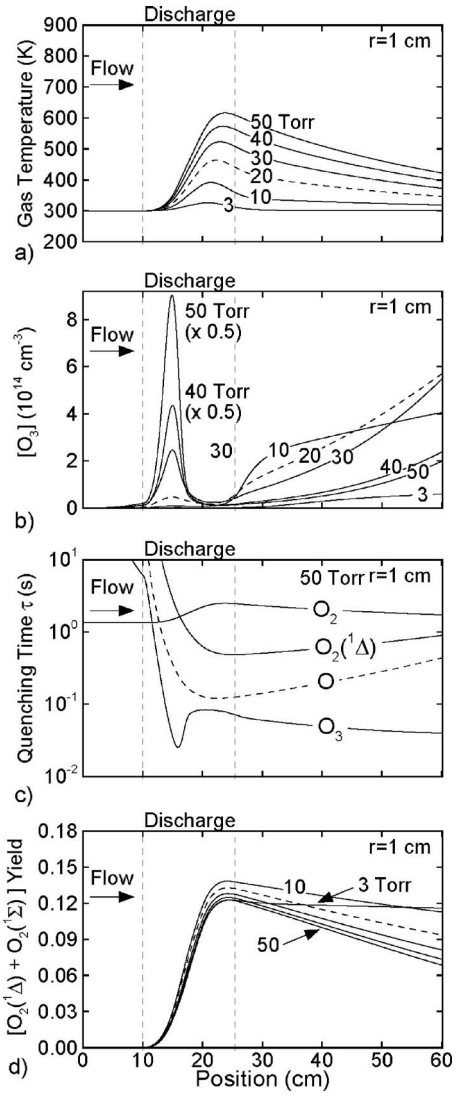

FIG. 8. Plasma and flow parameters for 3–50 Torr (α=0.9 eV/molecule, He/O_2=70/30) for a radius of 1 cm and a residence time of 60 ms. (a) Gas temperature, (b) O_3 density, (c) quenching times at 50 Torr, and (d) combined $O_2(^1\Delta)+O_2(^1\Sigma)$ yield. The smaller tube radius provides for higher rates of gas cooling which restores the ozone density in the afterglow. As such the yield for 50 Torr decreases from 10.8% to 7% compared to a 3 cm tube.

shown in Fig. 10. Yields and O_2^* densities decrease by approximately a factor of 2 at 50 Torr when including three-body quenching. For pressures greater than 20 Torr, three-body quenching by O atoms is commensurate with that by O_3, as shown in Fig. 10(d). Resolution of the value and temperature dependence of three-body quenching of $O_2(^1\Delta)$ by O atoms is clearly important to the pressure scaling of eCOIL devices. Alternatively, gas mixtures can be selected in which O atoms created by the discharge are scavenged and so minimize the influence of O atoms on quenching of $O_2(^1\Delta)$. Oxygen atoms are also efficient quenchers of the $I(^2P_{1/2})$ upper laser level, and so minimizing the O-atom density also directly aids in maintaining the inversion.

Many methods have been proposed to scavenge O atoms and so improve laser performance, such as coating of the tube walls with a HgO.[15] A practical and recently implemented method is to use small amounts of NO or NO_2 either in the initial gas flow or as additives downstream.[20] NO and NO_2 both rapidly react with O atoms in a chain reaction that has the net effect of converting O atoms to O_2. These reactions are

$$NO + O + M \rightarrow NO_2 + M, \tag{19}$$

$$NO_2 + O \rightarrow NO + O_2, \tag{20}$$

with rate constants of $1\times10^{-31}(T_g/300)^{-1.6}$ cm^6 s^{-1} and $4.21\times10^{-12}\exp(-273/T_g)$ cm^3 s^{-1}, respectively. By controlling the O-atom density in this manner, quenching by O_3 is also regulated as O atoms are the precursor to O_3 formation. NO addition has the added benefit of removing O_3 by

$$NO + O_3 \rightarrow O_2 + NO_2, \tag{21}$$

having a rate coefficient of $1.4\times10^{-12}\exp(-1310/T_g)$ cm^3 s^{-1}.

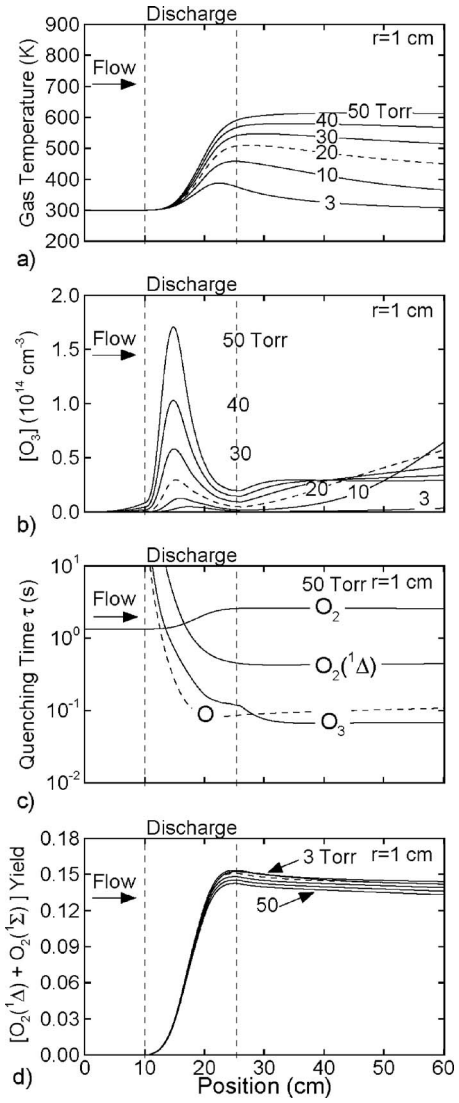

FIG. 9. Plasma and flow parameters for 3–50 Torr (α=0.9 eV/molecule, He/O_2=70/30) for a radius of 1 cm and a residence time of 7 ms. (a) Gas temperature, (b) O_3 density, (c) quenching times at 50 Torr, and (d) combined $O_2(^1\Delta)+O_2(^1\Sigma)$ yield. A smaller residence time results in lower gas temperature in the discharge region, but prevents rapid cooling in the afterglow. Yield is restored to 13.3%.

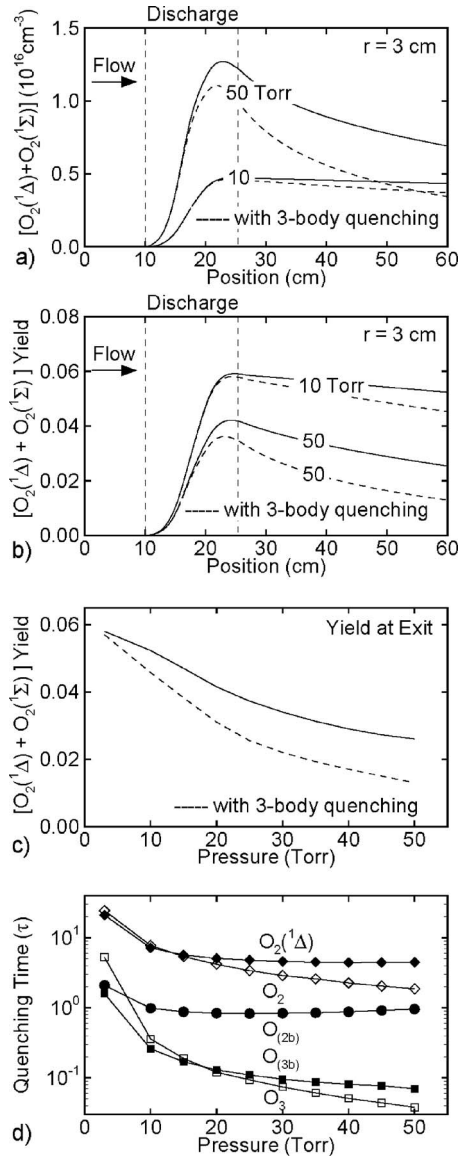

FIG. 10. Density of oxygen species (α=0.3 eV/molecule, He/O_2=70/30, r=3 cm) with and without three-body quenching with O atoms. (a) $O_2(^1\Delta)+O_2(^1\Sigma)$ for 10 and 50 Torr, (b) combined $O_2(^1\Delta)+O_2(^1\Sigma)$ yield for 10 and 50 Torr, (c) combined $O_2(^1\Delta)+O_2(^1\Sigma)$ yield as a function of pressure at the exit, and (d) quenching times. Accounting for three-body quenching results in substantial decrease in yield (dashed lines). Symbols $O_{(2b)}$ and $O_{(3b)}$ indicate atomic oxygen in two-body and three-body reactions.

The effect of NO addition in high pressure scaling when including three-body quenching by O atoms was investigated using the plug-flow model. Densities of oxygen species (O, O_3, and O_2^* and yield are shown in Fig. 11 as a function of pressure and inlet NO mole fraction. These quantities are at the exit of the flow tube. In the absence of NO, O and O_3 densities increase with pressure and saturate around 10–20 Torr. With these large densities of O and O_3 as quenchers, the density of O_2^* reaches a maximum between 10 and 20 Torr and slowly decreases at higher pressures. This quenching results in a monotonic decrease in yield.

With addition of up to 1% of NO, the exit densities of O and O_3 at pressures above 20–30 Torr are essentially eliminated. The reduction in these densities directly translates into less quenching and higher exit densities of $O_2(^1\Delta)$. With 1% NO, the absolute densities of $O_2(^1\Delta)$ increase with pressure and yields are largely restored. Although three-body quenching of $O_2(^1\Delta)$ is potentially an important process at high pressures, the consequences of this process can be minimized by managing the density of O atoms with small amounts of additives, such as NO or NO_2.

IV. CONSEQUENCES OF HYDRODYNAMICS ON PRESSURE SCALING

The results obtained using the plug-flow model provide insights into the kinetic processes that affect $O_2(^1\Delta)$ yields when increasing pressure. In this section additional considerations will be discussed with results from the 2D model that more realistically represent the electrical circuitry, electrode losses, uniformity, and flow considerations.

Another second order effect that may influence $O_2(^1\Delta)$ production is the discharge constriction commonly observed at higher pressures due to the smaller mean-free path of elec-

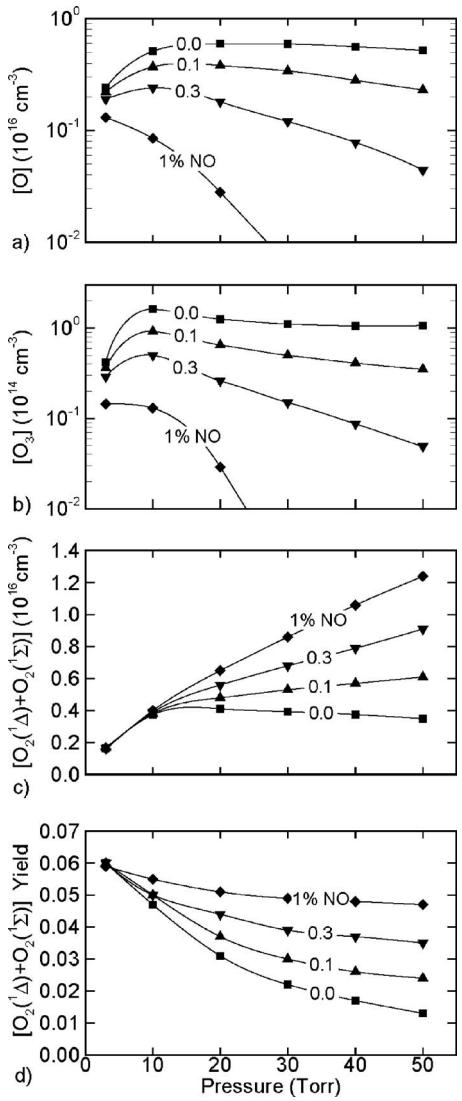

FIG. 11. Plasma properties at the exit of the flow tube (α =0.3 eV/molecule, He/O_2=70/30, r=3 cm) as a function of pressure and NO addition. Densities of (a) O, (b) O_3, and (c) $O_2(^1\Delta)+O_2(^1\Sigma)$, and (d) combined $O_2(^1\Delta)+O_2(^1\Sigma)$ yield. Three-body quenching by O atoms is included. Addition of small mole fractions of NO regulate the O-atom density and restores yield.

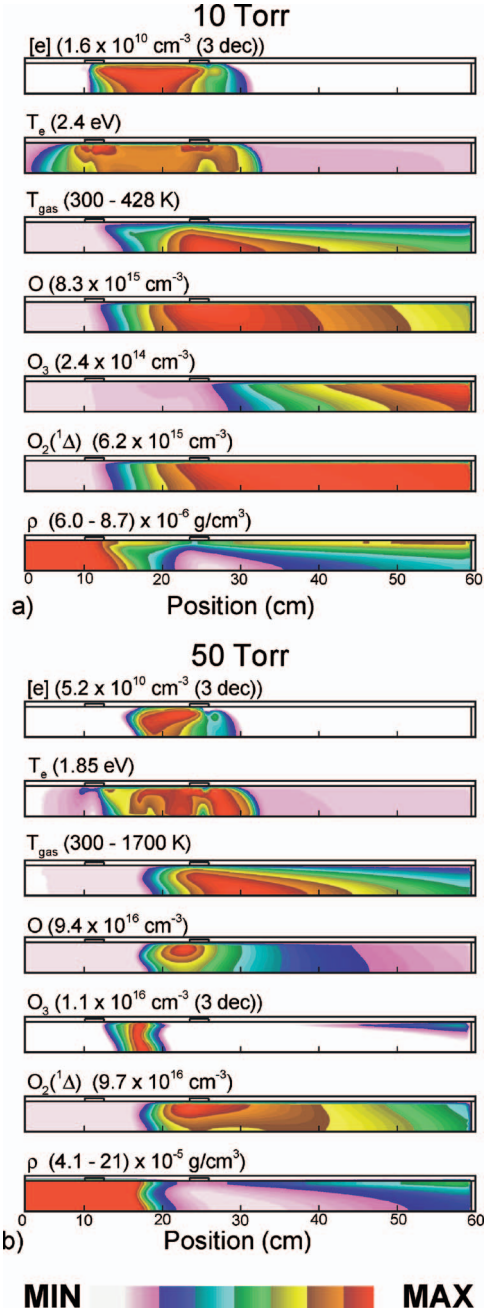

FIG. 12. (Color) Plasma parameters [electron density, electron temperature, gas temperature, and densities of O, O_3, and $O_2(^1\Delta)$, and total gas mass density] for (a) 10 and (b) 50 Torr (He/O_2=70/30, 25 MHz rf excitation, α=0.3 eV/molecule). All values are averaged over one rf period. The flow is from the left. The scales are linear with zero minimum values with the exception of T_g unless the number of decades is indicated for log plots. The maximum value is indicated in each figure. Discharge constriction at the higher pressure occurs near the downstream electrode.

trons and gas heating. The shorter mean-free paths result in electron-impact excitation occurring dominantly in regions of high electric field (that is, electron transport is local as opposed to nonlocal). Gas heating and the resulting rarefaction produce nonuniformities in gas density which even with uniform electric fields may produce nonuniform values of E/N (electric field divided by gas number density).

For example, plasma properties and the spatial distribution of species densities are compared in Fig. 12 for α =0.3 eV/molecule for moderate (10 Torr, 133 W) and high (50 Torr, 670 W) pressures. These results are averages over the 25 MHz cycle in the quasi-steady-state. (When comparing these results to those from the plug-flow model, recall that the values obtained from the plug-flow model are volume averages. The peak values as a function of radius in the 2D model, in many cases occurring on the axis, will be larger than those from the plug-flow model.) At 10 Torr the electron density is smoothly distributed between the electrodes with a peak value of 1.6×10^{10} cm^{-3}. The cycle averaged electron temperature is 1.9 eV in the bulk plasma, peaking at 2.4 eV near the electrodes. The dissociation fraction of the inlet O_2 is 4.5%, producing a peak O-atom density of 8.3×10^{15} cm^{-3}. The O atoms are progressively converted to O_3 as they flow towards the exit, producing an exit density of O_3 of 2.4×10^{14} cm^{-3}. The increase in gas temperature is about 130 K which decreases downstream where the O_3 density is highest. Due to the low gas temperature, $O_2(^1\Delta)$ quenching (mostly by ozone) is negligible.

At 50 Torr, the discharge becomes inhomogeneous with the highest electron density of 5×10^{10} cm^{-3} near the downstream electrode. The peak electron temperature drops to 1.85 eV. Due to recombination and Frank-Condon heating, the peak gas temperature increases to 1700 K. The rarefaction of the gas near the downstream electrode allows for higher proportional power deposition there. Oxygen molecules are more highly dissociated (10% fractional dissociation) producing a peak O-atom density of 9.4×10^{16} cm^{-3}. Due to the high temperature near the downstream electrode, O_3 produced in the upstream portion of the discharge is largely destroyed prior to leaving the discharge zone. The O_3 density is gradually restored downstream near the tube walls where the gas is coolest. The $O_2(^1\Delta)$ density maximizes in the discharge region where the power deposition is concentrated near the downstream electrode.

The reduced electric field E/N (electric field/gas number density) is not uniformly distributed over the discharge. The maximum values of E/N occur in the sheath regions near the electrode. However, at the pressures of interest, the majority of power deposition occurs in the bulk plasma where the electron density is maximum. In these volumes, typical values of E/N (averaged over a rf cycle) are 10–25 Td (1 Td $=10^{-17}$ V cm^2) with there being a tendency for the E/N to decrease with increasing pressure as diffusion losses decrease. For example, for $\alpha=0.3$ eV/molecule, E/N in the bulk plasma decreased from 25 Td at 3 Torr to 13 Td at 50 Torr. (These values do not significantly change for higher values of α.) Since the fractional power deposition into $O_2(^1\Delta)$ is maximum for $E/N\approx10$–15 Td, operating at higher pressures is kinetically more efficient since a larger fraction of power deposition is transferred to $O_2(^1\Delta)$.

Just as managing the O-atom and O_3 densities, and the gas temperature are important to scaling $O_2(^1\Delta)$ to higher pressures, so is managing the stability of the discharge. The transition from a diffusive and homogeneous discharge to one prone to instabilities or constricted states is not unusual when operating at higher pressures in electronegative gases.[12,15,19] At pressures lower than those associated with streamer propagation (as in corona discharges[24]) the onset of instabilities or constrictions results from a nonuniformity that produces local regions of higher power deposition or electron heating that diffusion is not able to disperse across a larger volume. That is, electron transport is local as opposed to nonlocal.

In the geometry investigated here, pressure scaling is ultimately limited by an instability initiated by discharge constriction which occurs between 40 and 50 Torr. This trend is shown in Fig. 13 where the electron density and power deposition are plotted for pressures from 3 to 50 Torr for $\alpha=0.3$ eV/molecule. The corresponding gas densities are shown in Fig. 14. Power deposition, diffusively distributed at 3 Torr, gradually constricts about the downstream electrode, producing a corresponding constriction in the electron density. This constriction results, in part, from an increasing degree of rarefaction in the total gas density in going from upstream to downstream as the gas heats. The lower gas density near the downstream electrode enables a higher conductivity and higher local power deposition.

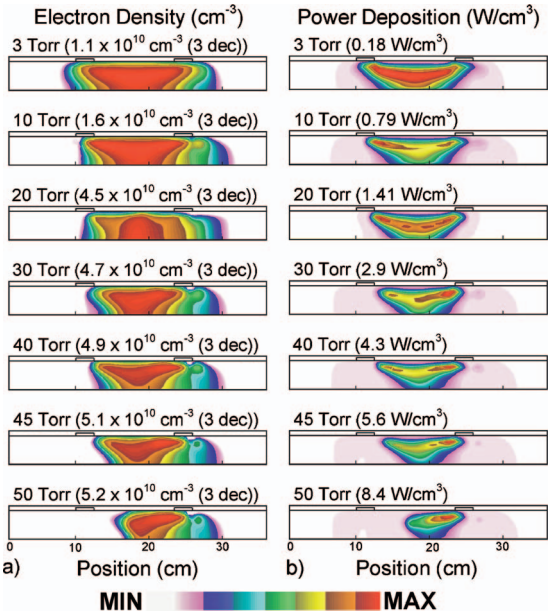

FIG. 13. (Color) Plasma parameters for pressures from 3 to 50 Torr ($He/O_2=70/30$, 25 MHz rf excitation, $\alpha=0.3$ eV/molecule). (a) Power deposition and (b) electron density. All values are averaged over one rf period. The flow is from the left. The scales are linear with zero minimum values unless the number of decades is indicated for log plots. The maximum value is indicated in each figure. Discharge constriction occurs near the downstream electrode due to rarefaction of the gas.

A measure of the onset of a constriction instability is the maximum value of the pressure normalized power deposition, P (W/cm^3 Torr). When keeping α constant and increasing pressure, and in the absence of constrictions, P should also remain a constant. The maximum value of P in the discharge, shown in Fig. 15, has a gradual increase from

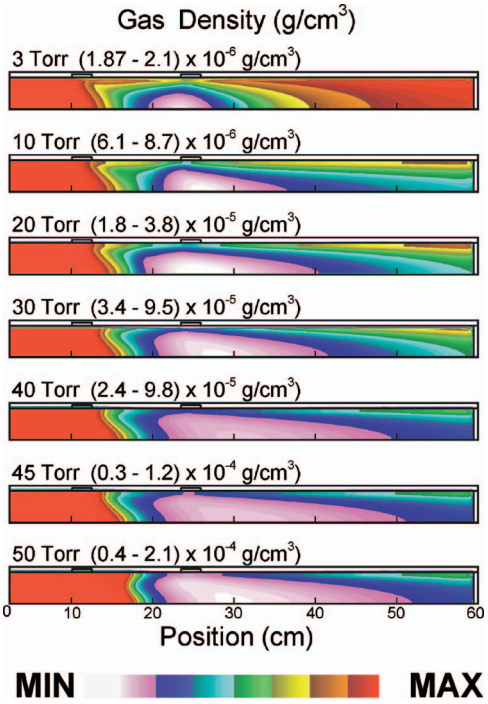

FIG. 14. (Color) Total gas density for pressures from 3 to 50 Torr ($He/O_2=70/30$, 25 MHz rf excitation, $\alpha=0.3$ eV/molecule). Significant rarefaction of the gas occurs near the downstream electrode.

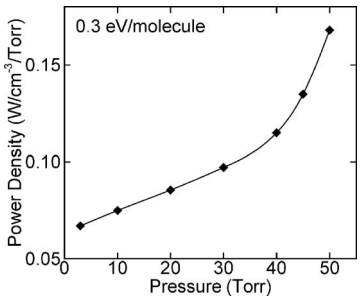

FIG. 15. Maximum value of the pressure normalized power deposition (W/cm^3 Torr) as a function of pressure ($He/O_2=70/30$, 25 MHz rf excitation, $\alpha=0.3$ eV/molecule). A transition from a uniform and homogeneous discharge to constricted discharge occurs between 40 and 50 Torr.

3 to 40 Torr, followed by a rapid increase above 40 Torr. This rapid increase indicates a constriction in the discharge.

The axial distributions of gas temperature and neutral oxygen species are shown in Figs. 16 and 17 for pressures from 10 to 50 Torr for $\alpha=0.3$ and 0.9 eV/molecule (133 and 400 W). The higher gas temperatures obtained at high pressures result in depletion of ozone in the afterglow. The maximum yields (15%–20% for $\alpha=0.3$ and 25%–30% for $\alpha=0.9$) are obtained at 50 Torr at the edge of the discharge zone. The yields then drop below 5% for $\alpha=0.3$ and below 10% for $\alpha=0.9$ due to quenching.

The hierarchy of the main quenchers of $O_2(^1\Delta)$ for 10, 30, and 50 Torr obtained with the 2D model is shown in Fig. 18 ($\alpha=0.3$ eV/molecule) and Fig. 19 ($\alpha=0.9$ eV/molecule). For the lower energy input (0.3 eV/molecule), O_3 is the main quencher in the afterglow up to 30–40 Torr. This result is basically the same as predicted by the plug-flow modeling. With increasing pressure and increasing absolute densities of atomic oxygen and $O_2(^1\Delta)$, quenching by these species begins to dominate. The pooling reaction,

$$O_2(^1\Delta)+O_2(^1\Delta)\rightarrow O_2(^1\Sigma)+O_2, \tag{22}$$

generates $O_2(^1\Sigma)$ as a product that is quenched to form $O_2(^1\Delta)$. For the higher energy input (0.9 eV/molecule), atomic oxygen and $O_2(^1\Delta)$ become the main quenchers in

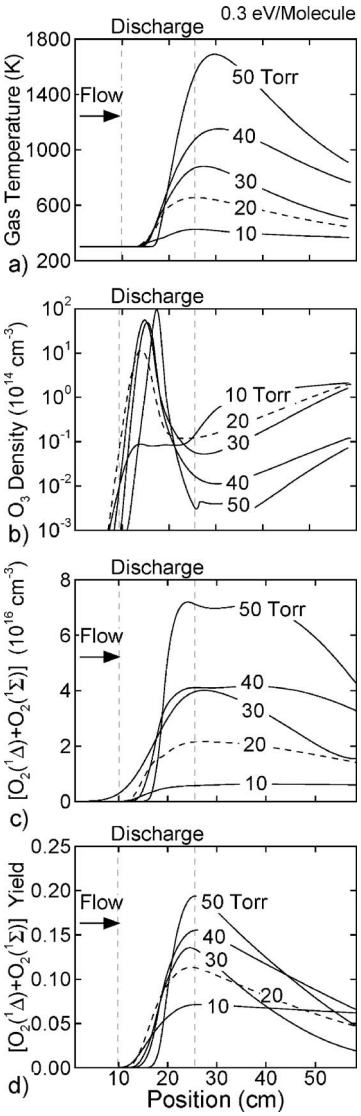

FIG. 16. Axial distribution of (a) gas temperature, (b) O_3 density, (c) $O_2(^1\Delta)+O_2(^1\Sigma)$ density, and (c) combined $O_2(^1\Delta)+O_2(^1\Sigma)$ yields ($He/O_2=70/30$, 25 MHz rf excitation) for $\alpha=0.3$ eV/molecule.

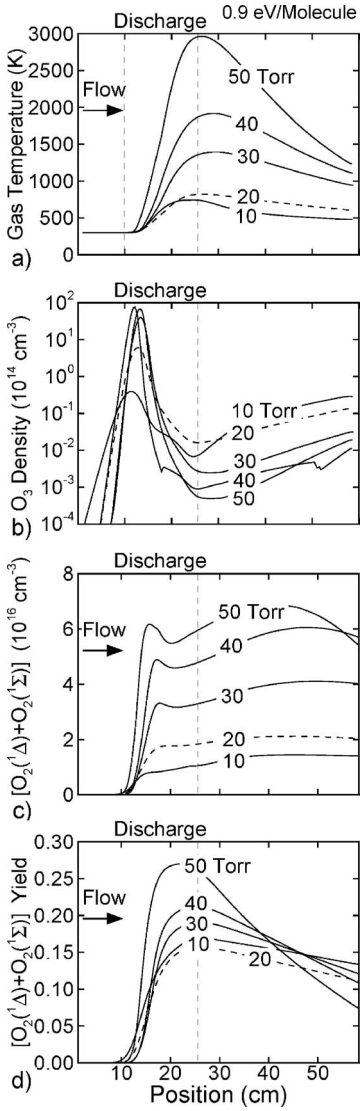

FIG. 17. Axial distribution of (a) gas temperature, (b) O_3 density, (c) $O_2(^1\Delta)+O_2(^1\Sigma)$ density, and (c) combined $O_2(^1\Delta)+O_2(^1\Sigma)$ yields ($He/O_2=70/30$, 25 MHz rf excitation) for $\alpha=0.9$ eV/molecule.

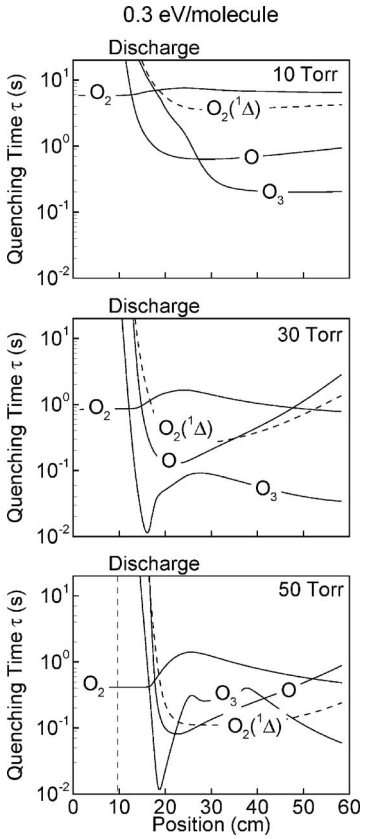

FIG. 18. Quenching times for $O_2(^1\Delta)$ for (a) 10, (b) 30, and (c) 50 Torr ($He/O_2=70/30$, 25 MHz rf excitation) for $\alpha=0.3$ eV/molecule. Up to 30–40 Torr ozone is the main quencher in the afterglow. With increasing pressure and increasing absolute densities of atomic oxygen and pooling reactions of $O_2(^1\Delta)$, quenching by these species begins to dominate.

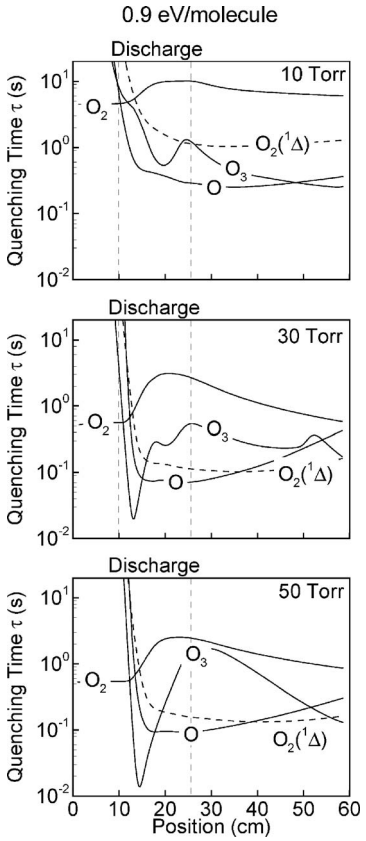

FIG. 19. Quenching times for $O_2(^1\Delta)$ for (a) 10, (b) 30, and (c) 50 Torr ($He/O_2=70/30$, 25 MHz rf excitation) for $\alpha=0.9$ eV/molecule. Quenching by atomic oxygen and pooling reactions of $O_2(^1\Delta)$ dominate.

the afterglow even for lower pressures, as shown in Fig. 19.

A summary of pressure scaling for $O_2(^1\Delta)$ production is shown in Fig. 20. $O_2(^1\Delta)$ densities and yields obtained from the 2D model as a function of power (for $\alpha=0.3$, 0.6, and 0.9 eV/molecule) are plotted for different pressures. These values are taken on the tube axis near the exit plane at 58 cm. Absolute $O_2(^1\Delta)$ production generally increases with power for any given pressure; however, it is not necessary maximum at the highest pressure. The yield of $O_2(^1\Delta)$ also increases with power for any given pressure; however, the yield at a given power generally decreases with pressure. These trends are largely a result of the increase in gas heating and influence of O_3, O, and $O_2(^1\Delta)$ quenching at higher pressures, and discharge constriction resulting from nonuniform rarefaction along the flow tube.

V. CONCLUDING REMARKS

Pressure scaling of the absolute densities and yields of $O_2(^1\Delta)$ in flowing He/O_2 plasmas was investigated using plug-flow and 2D plasma hydrodynamics models. We found that the densities and yields of $O_2(^1\Delta)$ can have significant sublinear scaling with pressure. Although yields may decrease with increasing pressure, absolute densities of $O_2(^1\Delta)$ typically do increase. Although these results depend on the layout of the electrodes and the aspect ratio of the flow tube more general conclusions can be made. Obtaining high yields of $O_2(^1\Delta)$ will require careful management of the O_3 density. Left unchecked, quenching of $O_2(^1\Delta)$ by the O_3 produced at high pressure is a rate limiting step. At higher energy densities and pressures, quenching by O atoms and en-

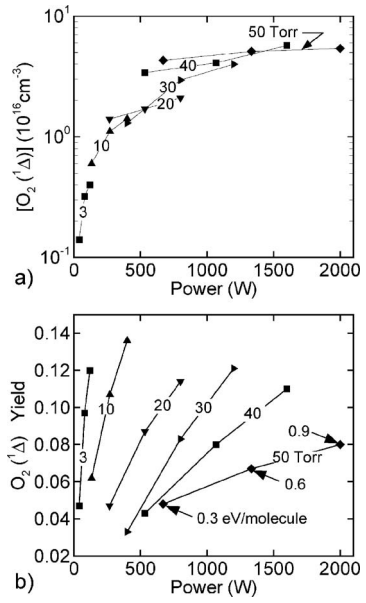

FIG. 20. Summary of pressure scaling of (a) $O_2(^1\Delta)$ densities and (b) yields as a function of power ($He/O_2=70/30$, 25 MHz rf excitation). Values are on the axis at 58 cm. $O_2(^1\Delta)$ production increases with increasing eV/molecule while yields at higher pressures may decrease.

ergy pooling with $O_2(^1\Delta)$ may also become important. This is particularly the case for possible three-body quenching involving O atoms, though the importance of this reaction can be minimized by managing the density of O atoms with additives such as NO. Pressure scaling also requires management of the gas temperature, as the rate of exothermic recombination reactions rapidly increase. Although the destruction of O_3 at higher temperatures is beneficial, in general an intermediate gas temperature is likely preferred. Discharge stability must also be managed and this will be highly temperature dependent. Nonuniform excursions of gas temperature in the plasma zone will produce nonuniform power deposition and constrictions near electrodes. As such, low aspect ratio, transverse electrodes allowing for more aggressive gas cooling and more distributed electric fields will likely be required for high pressure operation.

ACKNOWLEDGMENTS

This work was supported by the Air Force Office of Scientific Research and the National Science Foundation (CTS-0520368).

[1]W. E. McDermott, N. R. Pchelkin, D. J. Benard, and R. R. Bousek, Appl. Phys. Lett. **32**, 469 (1978).
[2]H. Fujii, S. Yoshida, M. Iizuka, and T. Atsuta, J. Appl. Phys. **67**, 3948 (1990).
[3]A. Elior, B. D. Barmashenko, E. Lebiush, and S. Rosenwaks, Appl. Phys. B: Lasers Opt. **B61**, 37 (1995).
[4]M. Endo *et al.*, IEEE J. Quantum Electron. **34**, 393 (1998).
[5]D. Furman, E. Bruins, V. Rybalkin, B. D. Barmashenko, and S. Rosenwaks, IEEE J. Quantum Electron. **37**, 174 (2001).
[6]J. Kodymova, O. Spalek, V. Jirasek, M. Censky, and G. D. Hager, Appl. Phys. A: Mater. Sci. Process. **77**, 331 (2003).
[7]J. Kodymova and O. Spalek, Jpn. J. Appl. Phys., Part 1 **37**, 117 (1998).
[8]A. A. Ionin, Y. M. Klimachev, A. A. Kotkov, I. V. Kochetov, A. P. Napartovich, L. V. Seleznev, D. V. Sinitsyn, and G. D. Hager, J. Phys. D **36**, 982 (2003).
[9]D. L. Carroll, J. T. Verdeyen, D. M. King, B. S. Woodard, L. W. Skorski, J. W. Zimmerman, and W. C. Solomon, IEEE J. Quantum Electron. **39**, 1150 (2003).
[10]Yu. V. Savin *et al.*, J. Phys. D **37**, 3121 (2004).
[11]A. N. Vasiljeva, K. S. Klopovskiy, A. S. Kovalev, D. V. Lopaev, Y. A. Mankelevich, N. A. Popov, A. T. Rakhimov, and T. V. Rakhimova, J. Phys. D **37**, 2455 (2004).
[12]A. Hicks, S. Norberg, P. Shawcross, W. Lempert, J. W. Rich, and I. Adamovich, J. Phys. D **38**, 3812 (2005).
[13]D. S. Stafford and M. J. Kushner, J. Appl. Phys. **98**, 073303 (2005).
[14]N. Yu. Babaeva, R. A. Arakoni, and M. J. Kushner, J. Appl. Phys. **99**, 113306 (2006).
[15]O. V. Braginsky, A. S. Kovalev, D. V. Lopaev, Yu. A. Mankelevich, O. V. Proshina, T. V. Rakhimova, A. T. Rakhimov, and A. N. Vasilieva, J. Phys. D **39**, 5183 (2006).
[16]O. V. Proshina, T. V. Rakhimova, O. V. Braginsky, A. S. Kovalev, D. V. Lopaev, Yu. A. Mankelevich, A. T. Rakhimov, and A. N. Vasilieva, J. Phys. D **39**, 5191 (2006).
[17]G. Bauville, B. Lacour, L. Magne, V. Puecha, J. P. Boeuf, E. Munoz-Serrano, and L. C. Pitchford, Appl. Phys. Lett. **90**, 031501 (2007).
[18]D. L. Carroll *et al.*, Appl. Phys. Lett. **85**, 1320 (2004).
[19]A. Hicks, Yu. G. Utkin, W. R. Lempert, J. W. Rich, and I. V. Adamovich, Appl. Phys. Lett. **89**, 241131 (2006).
[20]D. L. Carroll *et al.*, Appl. Phys. Lett. **86**, 111104 (2005).
[21]D. L. Carroll *et al.*, IEEE J. Quantum Electron. **41**, 1309 (2005).
[22]A. A. Ionin, I. V. Kochetov, A. P. Napartovich, and N. N. Yuryshev, J. Phys. D **40**, R25 (2007).
[23]K. S. Klopovskii, A. S. Kovalev, D. V. Lopaev, N. A. Popov, A T. Rakhimov, and T. V. Rakhimova, JETP Lett. **80**, 603 (1995).
[24]G. V. Naidis, J. Phys. D **38**, 2210 (2005).